ELSEVIER

Computation of phase equilibria by linear programming: A tool for geodynamic modeling and its application to subduction zone decarbonation

J.A.D. Connolly

Earth Sciences Department, Swiss Federal Institute of Technology, 8092 Zurich, Switzerland

Abstract

An algorithm for the construction of phase diagram sections is formulated that is well suited for geodynamic problems in which it is necessary to assess the influence of phase transitions on rock properties or the evolution and migration of fluids. The basis of the algorithm is the representation of the continuous compositional variations of solution phases by series of discrete compositions. As a consequence of this approximation the classical non-linear free energy minimization problem is trivially solved by linear programming. Phase relations are then mapped as a function of the variables of interest using bisection to locate phase boundaries. Treatment of isentropic and isothermal phase relations involving felsic and mafic silicate melts by this method is illustrated. To demonstrate the tractability of more complex problems involving mass transfer, a model for infiltration driven-decarbonation in subduction zones is evaluated. As concluded from earlier closed system models, the open-system model indicates that carbonates are likely to persist in the subducted oceanic crust beyond sub-arc depths even if the upper section of the oceanic mantle is extensively hydrated. However, in contrast to more simplistic models of slab devolatilization, the open-system model suggests slab fluid production is heterogeneous and ephemeral. Computed seismic velocity profiles, together with thermodynamic constraints, imply that for typical geothermal conditions serpentinization of the subducted mantle is unlikely to extend to >25 km depth and that the average water-content of the serpentinized mantle is <2 wt.%.
© 2005 Elsevier B.V. All rights reserved.

Keywords: phase equilibria; geodynamics; devolatilization; decarbonation; subduction; seismic tomography

1. Introduction

Comprehensive thermodynamic data for minerals [1–5] and silicate melts [6,7] provide a basis for constructing realistic models for rock behavior as a function of physical conditions. These models are of value in the classical inverse petrological problem whereby observed mineral assemblages are used to constrain the nature of geodynamic cycles. More recently, recognition of the influence of phase tran-

sitions on rock properties has led to the incorporation of detailed thermodynamic models for phase equilibrium effects in studies of seismic structure [8–10,5] and geodynamic cycles [11–14]. Such integrated approaches demand both a robust method for calculating phase equilibria and an efficient means of summarizing the resulting information. This paper presents a simple method that meets these demands.

The computational method outlined here employs free-energy minimization to map phase relations as a function of the variables of interest. The strategy can be split into two components: the minimization technique, which is the engine for the calculation; and the mapping strategy. Numerous workers have developed non-linear minimization techniques for the calculation of petrological phase equilibria [15–17,9]. A weakness of non-linear techniques is that identification of the stable mineral assemblage is probable, but not a certainty. Additionally, although non-linear techniques require little computational memory, they are slow and may fail to converge. An alternative to non-linear techniques is to approximate the continuous compositional variation of solution phases by sets of discrete compositions [18,19]. With this approximation, the identity and composition of the stable phases can be established by linear minimization techniques for which convergence to a global minimum is algorithmically certain [20]. The limitation of this method has been that accurate representation of the composition of complex solutions requires such a large number of discrete compositions that computer memory is taxed [21]. However, technological improvements have made minimizations with $>10^6$ discrete compositions feasible on ordinary desktop computers. A minimization on this scale requires ~ 1–10 s, thus linear optimization can be applied to map the equilibrium properties of a system as a function of arbitrarily chosen independent variables on a practical time scale.

Mapping is essentially independent of the minimization technique. Typically mapping strategies involve initial sampling the coordinate space of interest on a rectilinear grid. The initial grid may then be refined (C. de Capitani, personal communication, 2003) to accurately locate features such as phase boundaries or compositional isopleths. A drawback of many current implementations of such strategies is that provision is not made for storing all the information acquired during mapping. Thus, extraction of a particular feature such as a melt isopleth may involve repetition of the entire calculation. Recently, Vasilyev et al. [22] have proposed a scheme by which data obtained during mapping with non-linear minimization techniques can be stored through the use of continuous and discontinuous wavelets, thereby eliminating the need for repetitious calculations. Here it is shown that a simple bisection algorithm provides resolution and compression that is comparable to that obtained by the wavelet-based mapping.

Mapping phase relations by iterative application of a free-energy minimization is but one, and the crudest, of a variety of methods used in the geosciences [23]. The advantages of mapping strategies are that they are general with respect to the choice of mapping variables and that the resolution of the map is controlled by the user. Thus a low resolution map can be rapidly obtained for even the most complex systems. Such low resolution maps are sufficient for many geodynamic applications and are useful as a tool for the exploration of petrologic phase relations. Subsequently, low resolution maps can be refined to any level of accuracy required by specific applications. The methodology described here has been implemented in open source computer software and has been tested by application to various petrologic and geodynamic problems [10,24].

The first sections of this paper review the linearized formulation of the free energy minimization problem and describe the multi-level grid strategy used to map and recover phase relations and physical properties; the practical implementation of the algorithm and some applications with recent silicate melt models [6,7] are discussed in the next section; and the final section presents a minimal model for subduction zone decarbonation, a problem chosen to illustrate the feasibility of problems involving mass transfer. Subduction zone decarbonation has received attention because of its potential importance in the global carbon cycle [25–28], but because the decarbonation is coupled to much more voluminous dehydration, quantitative modeling of decarbonation is path dependent and therefore not easily quantified. To circumvent this complexity, initial attempts to quantify subduction zone decarbonation were based on a closed system

model that was argued to provide an upper limit for the efficiency of the subduction zone decarbonation process [29–31]. The open system model developed here, in which the fluids generated by devolatilization are permitted to migrate during subduction, is designed to test the validity of this argument. To this end an extreme and controversial scenario [32,33] is considered in which the subducted mantle is extensively hydrated.

For simplicity, the terminology appropriate for the analysis of an isobaric–isothermal closed chemical system is used here. In this case the Gibbs energy (G) is the thermodynamic function that is minimized during phase equilibrium calculations, the compositional variables describe the proportions of the different kinds of mass that may vary among the phases of the system, and the environmental variables are pressure (P) and temperature (T). However, the computational strategy is general and can be used for compositions that define the thermal and mechanical properties and environmental variables that relate to the chemistry [34].

2. Linear formulation of the minimization problem

The mimization problem is to find the amounts and compositions of the phases that minimize the Gibbs energy of a system (G^{sys}) at constant pressure and temperature [17,18]. The Gibbs energy of the system is expressed in terms of the Π phases possible in the system as:

$$G^{sys} = \sum_{i=1}^{\Pi} \alpha_i G^i, \qquad (1)$$

where G^i is the Gibbs energy of an arbitrary quantity, here chosen to be a mole, of the ith phase, and α_i is the amount of the phase, which is subject to the physical constraint

$$\alpha_i \geq 0, \qquad (2)$$

where in general $\alpha > 0$ if the phase is stable and $\alpha_i = 0$ if the phase is metastable, although in certain pathological cases the abundance of a stable phase may be zero. Mass balance further requires that the amounts of the components within the phases of the system

must sum to the corresponding amounts in the system, i.e.,

$$n_j^{sys} = \sum_{i=1}^{\Pi} \alpha_i n_j^i, \qquad j = 1 \ldots c, \qquad (3)$$

where c is the number of independent components, and n_i^j is the amount of the jth component in the ith phase.

The Gibbs energy of a solution phase is a nonlinear function of its composition and consequently the exact solution of phase equilibrium problems is complicated by the necessity of refining both the identities and compositions of the stable phases by iteration. To circumvent such complications, the compositional variation of a solution can be represented by a series of compounds, designated "pseudocompounds" [19,18]; defined such that each compound has the thermodynamic properties of the solution at a specific composition. From a computational perspective, each pseudocompound represents a possible phase in the formulation represented by Eqs. (1)–(3), but because there are no compositional degrees of freedom associated with the pseudocompounds the problem reduces to a linear optimization problem that can be solved by a standard procedure such as the Simplex algorithm [18] (a script that solves the linearized problem with the mathematical toolbox Maple is at www.perplex.ethz.ch/simplex.html). The input for the algorithm is the Gibbs energy and composition of the Π pseudocompounds chosen to represent the phases of interest and the output is the amounts of the p pseudocompounds that are stable in the approximated system, where in general $p \ll \Pi$.

It can be shown by thermodynamic argument [35] that if the possible phases of a system have no compositional degrees of freedom then the number of stable phases must be identical to the number of components. This argument precludes the unnatural situation that the composition of the system coincides exactly with that of a phase or a positive linear combination of fewer than c-phases. This situation poses semantic difficulties, but from a practical perspective it can be treated as an assemblage in which the amount of one or more of the stable phases is zero, hence the equality in condition (2). Thus, the solution of the approximated problem can always be expressed in terms of $p = c$ stable pseudocompounds, but it is

possible that more than one pseudocompound may represent a single true phase. In this case, the approximated properties of the true phase are obtained by combining the properties of the relevant pseudocompounds. Phase immiscibility may complicate matters because pseudocompounds may also represent two or more distinct phases represented by the same equation of state. To distinguish immiscible phases, the Euclidean distance

$$\delta = \sqrt{\sum_{j=1}^{c} \left(x_j^k - x_j^l\right)^2}$$

where x_j^i is the composition of component j in phase i, is computed between each pair of coexisting pseudocompounds that are represented by the same equation of state. If this distance is greater than a tolerance chosen so as to be greater than, but comparable to, the pseudocompound spacing, then the pseudocompounds are taken to represent immiscible phases. The ability to recognize and treat immiscibility is a particular advantage of the linear algorithm over non-linear algorithms that formulate the phase equilibrium problem in terms partial molar free energies. An additional complication in this class of non-linear algorithms, that the partial molar energy of a species becomes infinite as its concentration vanishes, is not an issue for algorithms formulated in terms of integral properties as done here. However, strongly non-ideal solution behavior may lead to scenarios in which it is desirable to resolve the compositional extremes of a solution with greater accuracy than is required for intermediate compositions. To accommodate this eventuality provision is made for both linear and non-linear discretization schemes.

The distinction between the exact and approximated problems is illustrated for a system with two possible phases β and γ (Fig. 1). For composition X^{sys}, the lowest energy of the true system is obtained by a positive linear combination of the energies β and γ, where the contacts of the common tangent between the free energy-composition surfaces of β and γ define the stable phase compositions (Fig. 1a). In the linearized formulation, β and γ are each represented pseudocompounds $\{\beta_1,\ldots, \beta_7, \gamma_1,\ldots, \gamma_8\}$ and for composition X^{sys} the algorithm would identify $\beta_4 + \gamma_6$ as the stable phase assemblage,
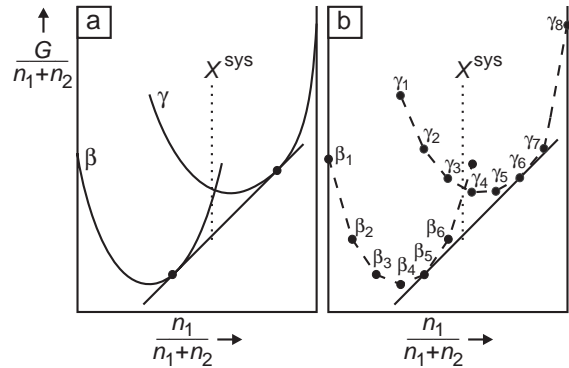

Fig. 1. Schematic isobaric–isothermal free energy-composition diagrams for a binary system illustrating the distinction between the non-linear solution to the phase equilibrium problem (a) and its linear approximation (b).

where β_4 and γ_6 approximate the stable compositions of β and γ with a maximum error corresponding to the compositional spacing of the pseudocompounds (Fig. 1b).

3. A multilevel grid strategy for mapping phase diagram sections

An effective minimization technique provides the basis by which phase relations and equilibrium system properties can be mapped in any linear or nonlinear section through the multidimensional P-T-X_1-$\ldots$-X_c phase diagram of a thermodynamic system. For simplicity, discussion is restricted here to two-dimensional phase diagram sections, although this is not a fundamental limitation of the method. Phase diagram sections are comprised by phase fields characterized by a particular phase assemblage, within these fields the chemical composition and physical properties of the stable phases may vary continuously, but are uniquely determined at any point. A consequence of the pseudocompound approximation is that the continuous compositional variation of the individual phases becomes discrete, so that the phase fields of a true section decompose into a continuous polygonal mesh of smaller pseudodivariant fields each of which is defined by a unique pseudocompound assemblage (Fig. 2a). The boundaries between adjacent pseudodivariant fields may represent either a true phase transformation (e.g., boundaries $\alpha + \gamma = \beta_4$ and $\alpha + \beta_3 = \beta_2$
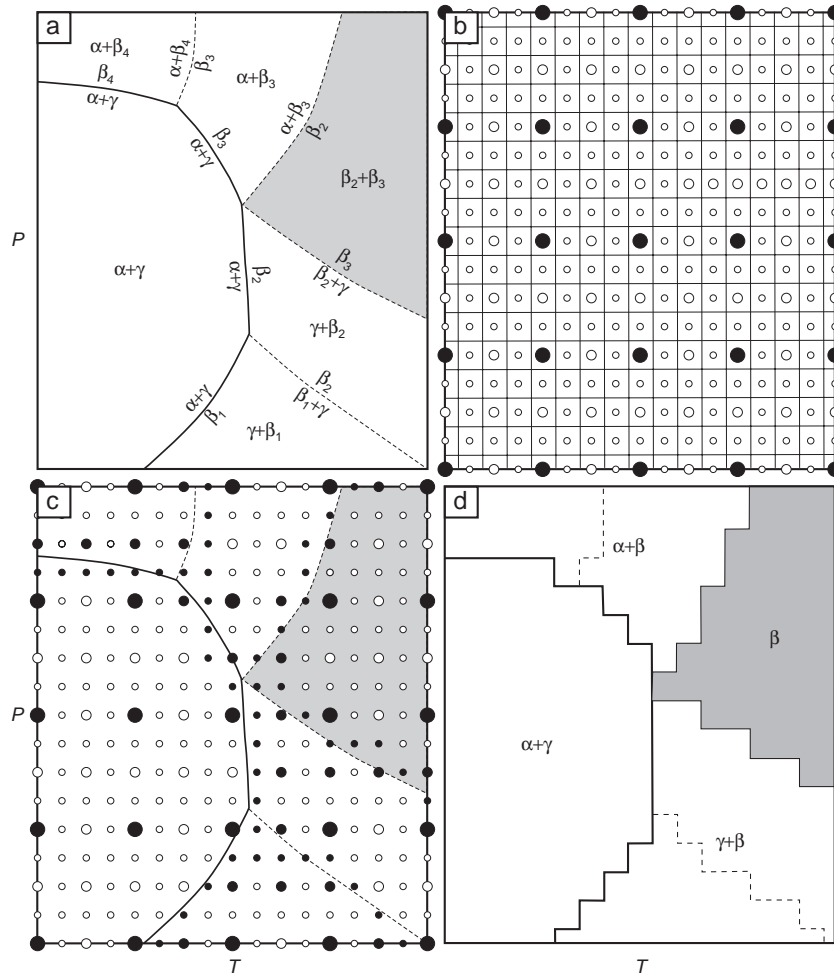
Fig. 2. Schematic phase pressure–temperature diagram section for a binary system in which phases α and γ are stoichiometric compounds and solution phase β is represented by pseudocompounds $\beta_1 \ldots \beta_4$. As a consequence of compositional discretization the true phase fields $\gamma + \beta$, β, and $\alpha + \beta$ decompose to smaller fields each defined by a unique pseudocompound assemblage (a) and boundaries between these fields are defined by reaction relationships. These boundaries may approximate either true phase boundaries (e.g., formation of β by continuous and discontinuous reactions $\beta_3 = \beta_2 + \gamma$ and $\beta_2 = \alpha + \gamma$, respectively) or homogeneous equilibration of a solution as a function or pressure and temperature (e.g., the boundary $\beta_1 = \beta_2 + \gamma$ approximates a compositional isopleth for the β in phase field $\gamma + \beta$). Phase relations are mapped by sampling on a four level grid as depicted in (b) with grid nodes at progressively higher levels indicated by circles of decreasing size. The nodes of this grid at which phase relations would be computed as dictated by the mapping strategy are indicated by filled circles in (c), the algorithmic logic assigns the assemblages associated with the open circles. The final map of the section (d) is constructed by assuming each node of the grid represents a finite area of the diagram.

in Fig. 2a) or simply the discretized variation in the composition of a solution (boundaries $\alpha + \beta_3 = \beta_4$ and $\beta_1 + \gamma = \beta_2$ in Fig. 2a), the latter effectively contouring the compositional variations of the corresponding true phase fields. An algorithm in which the polygonal mesh is traced directly to provide a map of the phase relations within a section is suggested by [23].

The limitations of this algorithm are that it becomes inefficient with the large numbers of pseudocompounds necessary to represent accurately the composition of complex solutions such as silicate melts and that it is difficult to use to map phase relations as a function of composition. Here a crude, but more robust, strategy that does not suffer these limitations

is proposed in which the structure of the polygonal mesh is mapped by sampling the equilibrium phase relations within a section on a multilevel Cartesian grid (Fig. 2). At the lowest level of resolution the grid has n_x and n_y sampling points on the horizontal and vertical axes. Grids of successively higher levels of resolution are generated by halving the nodal spacing, so that a grid at the rth level of resolution has $N_x = 1 + 2^{r-1}(n_x - 1)$ and $N_y = 1 + 2^{r-1}(n_y - 1)$ nodes along its horizontal and vertical axes (Fig. 2b). The grid nodes at each level of resolution define a mesh of rectangular cells, such that each cell contains four cells at the next higher level. In the first iteration, the stable pseudocompound assemblages are determined at all the nodes of the lowest level (filled circles, Fig. 2b). If the same assemblage is stable at four corners of a cell, then the assemblage is assumed to be stable at the grid points at all levels of resolution contained by cell. Likewise, if two or three nodes represent the same assemblage, then all higher resolution grid points that lie along the line or within the triangle connecting the homogeneous nodes are assumed to represent the assemblage. Partially and entirely heterogeneous cells are marked for investigation in the next step, in which each of these marked cells is split into four cells at the next higher level. The stable assemblages at any of these nodes that are not known from the previous step are determined by free energy minimization, and heterogeneous cells are again marked for investigation. This process is repeated until the highest level is reached, resulting in a grid with an effective resolution of $N_x \times N_y$ points (Fig. 2c). A continuous map of the phase relations can then be reconstructed by associating a representative area with each point of the $N_x \times N_y$ grid (Fig. 2d). The multilevel grid strategy can be generalized for multidimensional problems, and in comparison to the wavelet-based strategy advocated in [22], has the advantage of simplicity with comparable efficiency.

In the ideal case that the boundaries to be mapped are monotonic functions of the map coordinates the accuracy of the multilevel grid is identical to that obtained by brute force mapping on a $N_x \times N_y$ grid. More generally, the cost for the efficiency of the multilevel strategy in terms of the number of minimizations is that incursions on the scales of the lower levels of the grid may be missed

entirely. Thus, the grid spacing at the lowest level should be chosen so as to reduce the importance of such errors to an acceptable level. For the illustration (Fig. 2), mapping all features of the phase diagram section at the highest level of resolution would require 289 minimizations; whereas use of a three-level grid reduces the number of minimizations required to 91. For purposes of solely depicting phase relations, it is not necessary to resolve features that do not correspond to true phase boundaries, e.g., internal boundaries $\alpha + \beta_3 = \beta_4$ and $\beta_1 + \gamma = \beta_2$ in Fig. 2a. In such cases, the algorithm is modified so that pseudocompounds that represent the same phase are considered to be identical for purposes of mapping. Making this simplification in the illustration (Fig. 2) reduces the required number of minimizations from 91 to 73, but in real problems the simplification generally results in a more substantial saving. The data that must be stored for post-processing can also be reduced by discarding results from minimizations that yield replicate assemblages. In the example (Fig. 2c), compression by this method reduces the number of grid points for which the full data is stored to only 6 points, although a total of 86 nodal locations are required to define the boundaries.

Properties such as mineral proportions and compositions, density, entropy, enthalpy, and seismic velocities are recovered from the data stored for each minimization. Because these properties vary continuously as function of the grid variables, properties at any arbitrary sampling point are estimated by linear interpolation or extrapolation from the three nearest grid points at which the assemblage at the sampling point is stable. For such purposes, the compression strategy outlined above is modified, or entirely eliminated, to reduce the distance over which interpolation is done. If an assemblage is stable at fewer than three grid points physical, then properties are estimated by extrapolation. For this purpose, the properties and their derivatives are estimated by finite difference from the Gibbs function.

4. Implementation and limitations of the algorithm

The algorithm is implemented as an option, referred to as "gridded minimization", in a collection

of FORTRAN programs for the calculation and graphical representation of phase equilibria named Perple_X. Grid variables may be chosen as pressure, temperature, pressure as a function of temperature (or vice versa), chemical potentials, phase compositions and bulk composition (which may define mechanical and thermal state as well as chemical composition [34]). Bulk compositional variables may be specified to define a closed composition space such that the molar composition of the system ($\overrightarrow{C}_{system}$) is:

$$\overrightarrow{C}_{system} = \sum_{i}^{n} X_i \overrightarrow{C}_i, \quad \sum_{i}^{n} X_i = 1, \quad 0 \leq X_i \leq 1$$

or an open space such that:

$$\overrightarrow{C}_{system} = \overrightarrow{C}_0 + \sum_{i}^{n-1} X_i \overrightarrow{C}_i, \quad 0 \leq X_i \leq 1$$

where the $\overrightarrow{C}_i$ are $n \leq c$ arbitrarily specified compositional vectors.

Perple_X, including documentation, can be copied via www.perplex.ethz.ch. The programs can be used with most recent geological thermodynamic databases [1–5]. Because the programs are open source, they can be modified to accommodate mineral equations of state that have not been anticipated in the present code or for other specialized purposes. Graphical output from the package is written in interpreted PostScript that can be imported into commercial graphical editors. Alternatively, output from Perple_X may be imported as look-up tables for geodynamic calculations or into analytical toolboxes such as MatLab.

Linearization essentially reduces the numerical aspects of the phase equilibrium problem to an algebraic problem without path dependence and in this regard the claim of algorithmic certainty is legitimate. However, the method provides an exact solution to an
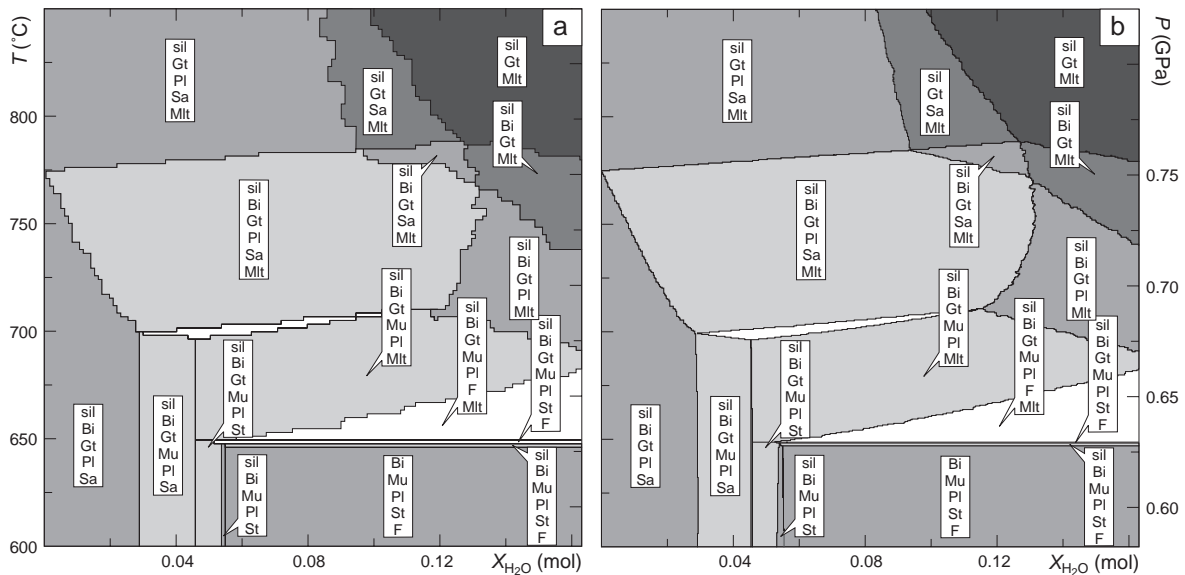

Fig. 3. Phase relations along a Barrovian geotherm (25 °C/km) as a function of water content for a pelitic composition (0.021 Na_2O, 0.038 K_2O, 0.008 CaO, 0.050 MgO, 0.096 FeO, 0.189 Al_2O_3, 1.021 SiO_2 in molar units) modified from [54], the maximum molar water content represented on the diagram corresponds to 5 wt.% H_2O. See Table 1 for notation and data sources. In the low resolution calculation (a) compositions were resolved at <0.1 mol% increments with 3×10^5 pseudocompounds on a 5-level grid with 10×10 nodes at the lowest level (145×145 nodes at the highest level). The calculation required 0.5 h on a 1.6 GHz computer and involved 1962 minimizations (1 s/minimization) out of the 21,025 (9.3%) necessary to achieve the same resolution on a regular grid. For the high resolution calculation (b), which required 33 h to do 10,122 minimizations (12 s/minimization) out of 390,625 (2.5%), phase compositions where discretized with an accuracy of better than 0.03 mol% (generating 7×10^6 pseudocompounds) on a 5-level grid with 40×40 nodes at the lowest level (625×625 nodes at the highest level). See www.perplex.ethz.ch/perplex_tx_pseudosection.html for computational details.

Table 1
Phase notation and thermodynamic data sources

Symbol	Phase	Formula	Source
A	Phase A	$Mg_{7x}Fe_{7(1-x)}Si_2O_8(OH)_6$	[24]
Atg	Antigorite	$Mg_{48x}Fe_{48(1-x)}Si_{34}O_{85}(OH)_{62}$	[24]
Bi	Biotite	$KMg_{(3-w)x}Fe_{(3-w)(1-x)}Al_{1+2w}Si_{3-w}O_{10}(OH)_2, x+y \leq 1$	[58]
Chl	Chlorite	$Mg_{(5-y+z)x}Fe_{(5-y+z)(1-x)}Al2_{(1+y-z)}Si_{3-y+z}O_{10}(OH)_8$	[59]
Coe	Coesite	SiO_2	
Cpx	Clinopyroxene	$Na_{1-y}Ca_yMg_{xy}Fe_{(1-x)y}Al_ySi_2O_6$	[60]
F	Fluid	$(H_2O)_x(CO_2)_{1-x}$	[41]
Fsp	Feldspar	$K_yNa_xCa_{1-x-y}Al_{2-x-y}Si_{2+x+y}O_8, x+y \leq 1$	[61]
Gt	Garnet	$Fe_{3x}Ca_{3y}Mg_{3(1-x-y)}Al_2Si_3O_{12}, x+y \leq 1$	[3]
Ky	Kyanite	Al_2SiO_5	
Lw	Lawsonite	$CaAl_2Si_2O_7(OH)_2 \cdot (H_2O)$	
M	Magnesite	$Mg_xFe_{1-x}CO_3$	[3]
Mu	Mica	$K_xNa_{1-x}Mg_yFe_zAl_{3-2(y+z)}Si_{3+y+z}O_{10}(OH)_2$	[3]
Melt	Melt	Na–Mg–Al–Si–K–Ca–Fe silicate melt	[7]
Mlt	Melt	Na–Mg–Al–Si–K–Ca–Fe hydrous silicate melt	[6]
Ol	Olivine	$Mg_{2x}Fe_{2(1-x)}SiO_4$	[3]
Opx	Orthopyroxene	$Mg_{x(2-y)}Fe_{(1-x)(2-y)}Al_{2y}Si_{2-y}O_6$	[60]
Pl	Plagioclase	$Na_xCa_{1-x}Al_{2-x}Si_{2+x}O_8$	[62]
San	Sanidine	$Na_xK_{1-x}AlSi_3O_8$	[63]
St	Staurolite	$Mg_{4x}Fe_{4(1-x)}Al18Si_{7.5}O_{48}H_4$	[3]
Stv	Stishovite	SiO_2	
Ta	Talc	$Mg_{(3-y)x}Fe_{(3-y)(1-x)}Al_{2y}Si_{4-y}O_{10}(OH)_2$	[3]
Tr	Amphibole	$Ca_{2-2w}Na_{z+2w}Mg_{(3+2y+z)x}Fe_{(3+2y+z)(1-x)}Al_{3-3y-w}Si_{7+w+y}O_{22}(OH)_2, w+y+z \leq 1$	[64]

Unless indicated otherwise thermodynamic data was taken from [3] (revised 2002). The compositional variables w, x, y, and z may vary between zero and unity and are determined as a function of pressure and temperature by free-energy minimization. Thermodynamic data for the iron end-members for antigorite and phase-A were estimated as described in [24].

approximated problem; thus a critical issue is whether the requisite accuracy, which is controlled entirely by the user, can be achieved without making the method impractical. Comparisons with non-linear solvers (e.g., THERMOCALC [36]) have confirmed that the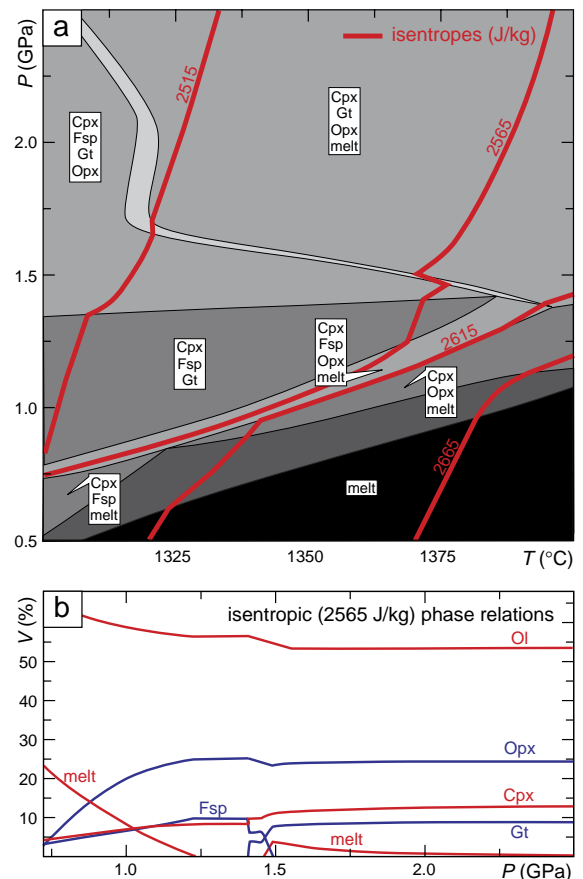 linear and non-linear methodologies converge at levels of approximation that make the linear method attractive. A specific example, in which mineralogies and seismic velocities for the upper mantle computed by a non-linear method [5] are compared to those obtained with Perple_X is provided at www.perplex.ethz.ch/bench.html.

4.1. Examples

To illustrate the tractability of more challenging geological problems by the proposed method, it is applied here to calculate melting relations under crustal and mantle conditions. In crustal melting scenarios, pressure and temperature are dictated by external factors, so that the major source of variability is the availability of water. In this context, a phase diagram section that depicts phase relations as a function of conditions along a geothermal gradient and water content is useful. Fig. 3 shows low and high resolution versions of such a calculation. Comparison of the calculations demonstrates that, in light of typical geological and thermodynamic uncertainties, low resolution calculations capture the essential features of the phase relations and that the virtue of high resolution calculations is largely aesthetic. The low resolution calculation illustrates the two distinct sources of discretization error associated with the algorithm. The relatively large scale periodic irregularities, such as those along the left boundary of the sil+Gt+Sa+Mlt field (at ∼800 °C, Fig. 3a, see Table 1 for phase notation), are due to discretization of the melt composition; whereas the individual steps reflect the resolution of the mapping. Thus, an increase in grid

resolution, without a commensurate increase in the resolution of melt composition (i.e., an increase in the number of pseudocompounds used to represent the melt), has little value because it would resolve artifacts of compositional discretization. This complexity is a drawback of the method, but is not a limitation of mapping strategies that employ non-linear solvers [17,22]. An additional limitation of the method is that the number of pseudocompounds necessary to obtain a uniform compositional resolution δ for a given solution is $2(2\delta)^{1-c}$, therefore to resolve melt compositions at 0.03 mol% increments as in Fig. 3b would require $\sim 10^{12}$ pseudocompounds. Thus, in practice, an initial low resolution calculation must be done to establish the range of melt compositions, which is then used to define the range resolved at high resolution in a subsequent calculation. Automation of this refinement procedure is a goal for future work. A more fundamental limitation of mapping

Fig. 4. Melting phase relations for a simplified version of the LOSIMAG [45] mantle composition (molar composition: 0.707 SiO_2, 0.037 Al_2O_3, 0.0971 FeO, 0.867 MgO, 0.053 CaO, 0.005 Na_2O, 0.001 K_2O) (a). Olivine is stable in all phase fields, other phases are stable as indicated, see Table 1 for phase notation and data sources. Red curves depict isentropic decompression paths, labeled by entropy (J/kg), as recovered from the calculation. (b) Mineral and melt modes as a function of pressure along the 2565 J/kg isentrope. Thermodynamic end-member data for the melt model [7] were corrected for the appropriate reference state [3]. Because the solution models employed for the present calculation differ from those used in the pMELTS software [7], the results differ in details from those obtained with pMELTS. Absence of a spinel stability field reflects the absence of Cr from the chemical model. Likewise the stability of trace amounts of sanidine (Fsp) at high pressure is probably an artifact of the absence of a model for K-solution in the remaining subsolidus silicates. Phase compositions where discretized with an accuracy of better than 3 mol% (generating 8×10^5 pseudocompounds) on a 3-level grid with 40×40 nodes at the lowest level (157×157 nodes at the highest level). Because internal phase boundaries were defined, the computation required a high proportion of minimizations (70%, 0.5 s/minimization on a 1.5 GHz computer) compared to the calculations depicted in Fig. 3. See www.perplex.ethz.ch/perplex_adiabatic_crystallization.html for computational details.

strategies is that they cannot unequivocally identify geometrically degenerate phase diagram features such as univariant and invariant phase fields, e.g., it is not possible to distinguish a line from a narrow two dimensional field. The apparently invariant water-saturated phase relations depicted at ~650 °C in Fig. 3 illustrate this type of ambiguity, the absence of any detectable temperature dependence suggests these phase relations are truly invariant, but is not a conclusive diagnostic.

In many mantle scenarios, the melting process is best approximated as adiabatic, thus temperature is a dependent property and closed system phase relations should be computed to mimimize enthalpy at constant entropy, mass, and pressure. Such computations are possible in existing programs [34,37]; however, an alternative approach (cf. [5]) is illustrated (Fig. 4) in which isentropic geotherms are recovered from the computed phase relations for an anhydrous mantle bulk composition. Properties such as phase proportions (Fig. 4b), enthalpy, and seismic velocities along any adiabatic path of interest can then be recovered from the data stored for the calculation as a function of temperature and pressure. The inflection in the mantle solidus to higher temperature at low pressure (Fig. 4a) reflects the importance of plagioclase as a host for alkali elements and has the interesting implication that melts produced near the garnet lherzolite solidus may freeze during adiabatic upwelling of the mantle as occurs along the calculated 2665 J/kg isentrope (Fig. 4b, [cf. [38]]).

5. Phase fractionation and open system models

A limitation in the geological application of the foregoing models is that although they assume a closed chemical system they demonstrate the generation of physically mobile phases, i.e., melt and aqueous fluid, the existence of which is likely to lead to violation of the closed system assumption. Formation of a refractory phase that, once formed, ceases to equilibrate with the remainder of the system has the same effect as physically removing the refractory phase from an otherwise closed system. The treatment of such problems requires the knowledge of the variations in the external variables that induce the growth of the mobile or refractory phase as well as a model

for the physical process of fractionation. In practice the continuous variation in physical conditions is discretized, and after each discrete variation the state of the system is assessed to determine the amount of the fractionated phase (e.g., [37,39]). In the case of a mobile phase the physical domain can also be discretized to assess the effect of the migration of the mobile phase. The strategy proposed here provides an efficient means by which phase equilibrium constraints can be actively or passively coupled to geodynamic models that predict variations in the physical conditions of a system. Here a simple model to assess the stability of carbonate in subducted oceanic crust is considered to illustrate such calculations.

5.1. Geological scenario and model for subduction zone decarbonation

Because pure decarbonation reactions occur at extraordinarily high temperature, the release of CO_2 beneath island-arc systems is inextricably tied to the dehydration of hydroxylated and/or hydrous silicates that decompose at sub-arc and shallower depths [e.g, [40]]. The presence of water influences carbonate stability in two distinct ways: coexistence of carbonate and hydrous silicates is limited by eutectic-like reactions that generate relatively CO_2-rich, H_2O–CO_2 fluids [41]; and the finite solubility of carbonate in water can cause decarbonation even in the absence of hydrous silicates. The former mechanism requires relatively high bulk H_2O/CO_2 ratios, thus it is suppressed if water generated by low-temperature dehydration leaves the system. The latter mechanism is dependent on the amount of CO_2 required to saturate aqueous fluid. Since this amount is small at the temperatures of interest, the mechanism is only likely to be important if large amounts of fluid generated by deeper dehydration infiltrate the subducted oceanic crust.

Under the assumption that the infiltration mechanism was insignificant, [10,30,31] argued that closed system models provide a conservative estimate for carbonate stability within the slab, because such models maximize the H_2O/CO_2 ratio of the crustal rocks. To test this assumption, here it is assumed that the lower crust and upper mantle are extensively hydrated at shallow depths (Fig. 6). Physical conditions are then varied stepwise to simulate the subduction process and after each step the equilibrium mineralogy of
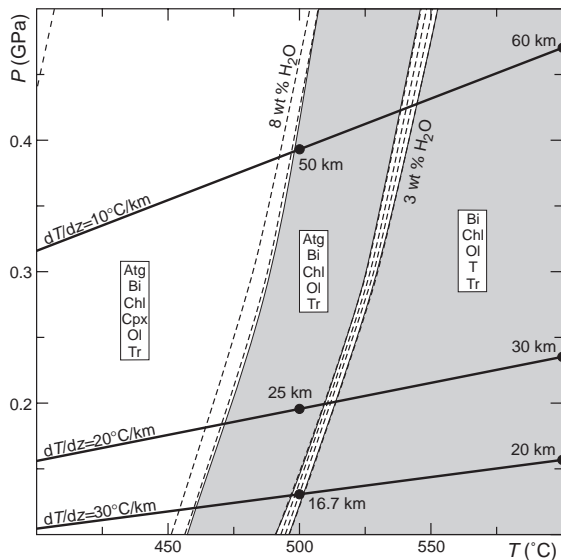
Fig. 5. Calculated water-saturated mineralogy for the LOSIMAG mantle composition (Fig. 3) contoured at 1 wt.% intervals for water content (dashed curves); see Table 1 for phase notation and data sources. If mantle serpentinization at oceanic trenches occurs by penetration of sea water through open fractures, then the maximum water pressure is limited by hydrostatic conditions (computed for an average fluid density of 800 kg/m^3). Assuming fluid pressure dictates the thermal stability of serpentinite (Atg) [46], the maximum depth of serpentinization is limited by the intersection of the relevant hydrothermal gradient (heavy lines) with the talc (T) stability field. This argument suggests that evidence for deep mantle serpentinization [32] should correlate with unusually cool slab geotherms.

lithospheric slab is computed from the base upward, assuming that the local mineralogy equilibrates with all the fluid generated at greater depth. An average composition for the upper 500 m of oceanic basaltic crust [42] is taken as representative of the upper 2 km of the model crust, this is underlain by a 4 km section with gabbroic composition [43], modified to contain 1.5 wt.% water to represent the effects of lower crustal hydrothermal alteration [44]. The LOSIMAG composition [45] is taken to represent oceanic mantle with the addition of 4 wt.% water as a generous estimate for the amount of water hypothesized to enter the mantle at oceanic trenches [24,32]. The vertical extent of mantle hydration can be constrained by observing that if mantle hydration occurs by penetration of sea water through a connected fracture network, the maximum fluid pressure is limited by the hydrostatic condition for the fluid. This fluid pressure is the

relevant pressure [46] for establishing the maximum thermal stability of serpentinite, thus taking antigorite as a proxy for the properties of serpentine [3] and a geothermal gradient of 20 °C/km, such as characteristic of the trench environment [47,24], it is found that lithospheric serpentinization may extend to 20–25 km depth (Fig. 5). Since this estimate includes the oceanic crust, the vertical extent of hydrated mantle is taken to be 18.5 km. Kinetic effects or the presence of salts in the fluid would decrease this depth limit, whereas a cooler geothermal gradient, as might be expected for greater slab ages, would extend it.

For purposes of the model, geothermal conditions (Fig. 7a) are chosen to represent subduction of a young (40 Ma) slab at a rate of 10 cm/y. The choice of a slab age and subduction rate that deviate somewhat from the global averages ($\sim$55 Ma and $\sim$6 cm/y, respectively) maximizes mantle dehydration at subarc depths [24], thereby maximizing the efficiency of infiltration-driven decarbonation. The model configuration (Fig. 6) implies a global influx of $\sim$0.55 Gt CO_2/y (global rates based on a global subduction rate of 2.7 km^2/y [24]) into subduction zones that is nearly
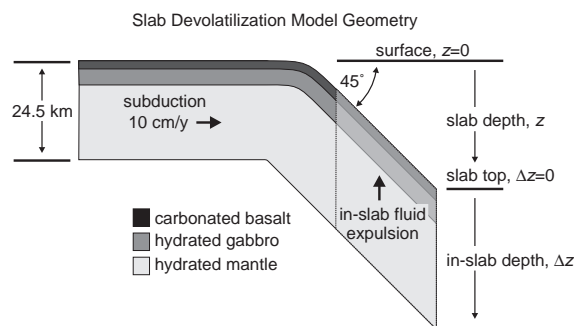

Fig. 6. Subduction zone devolatilization model configuration. The lightly shaded trapezoidal region corresponds to the rectangular coordinate frame of Fig. 7a, Figs. 8 and 9. Physical conditions are based on a numerical simulation of subduction of young (40 Ma) oceanic lithosphere ("slab") at 0.1 m/y and at 45° with respect to the earth's surface. The initial molar compositions of the upper crust (0–2 km; 0.153 H_2O, 0.069 CO_2, 0.784 SiO_2, 0.157 Al_2O_3, 0.143 FeO, 0.167 MgO, 0.236 CaO, 0.034 Na_2O, 0.006 K_2O, [42]), lower crust (2–6 km; 0.083 H_2O, 0.903 SiO_2, 0.140 Al_2O_3, 0.097 FeO, 0.304 MgO, 0.194 CaO, 0.020 Na_2O, 0.001 K_2O, [43,44]) and mantle (6–18.5 km; 0.211 H_2O, 0.707 SiO_2, 0.037 Al_2O_3, 0.0971 FeO, 0.867 MgO, 0.053 CaO, 0.005 Na_2O, 0.001 K_2O, [45]) were chosen so that the equilibrium mineralogies for the three lithologies are isochoric at the initial condition, no corrections were made for compaction or compression. Because of the slab dip, the vertical thickness of the modeled portion of the slab is 34.65 km.

twice that obtained if the carbonate budget is estimated by taking into account the sediment carbonate budget [48], but assuming that no significant carbonate is present at depths beyond 500 m within the basaltic section of the crust.

Simplified models that assume fluid saturation or closed system behavior (e.g., [49,50,30,47]) generally exclude the possibility that regions of the volatile-bearing oceanic lithosphere may be thermodynamically undersaturated with respect to a fluid phase. The open system model illustrates that the existence of such regions, in conjunction with the assumption of pervasive fluid flow, can lead to behavior in which fluids cascade between different levels of the slab (Figs. 7c, 8 and 9a) and then disappear as a consequence of hydration reactions. Even if fluid flow derived from

the mantle is disregarded, the open system model suggests that if slab fluid expulsion is efficient, as implicit in the formulation, then fluids are distributed more sporadically than previously inferred.

In the present model (Figs. 7c, 8), devolatilization commences at 96 km depth and is confined to the upper crustal section of the slab until a depth of 136 km. The negligible amount of decarbonation that occurs during this stage (Fig. 9b) demonstrates that, compared to the closed system model [30], open system behavior increases the stability of carbonate mineralogies in settings where the fluid is derived largely from the carbonate-bearing lithology. In the depth range 136–156 km, dehydration of serpentine and chlorite in oceanic mantle is a voluminous source of water-rich fluids. The near coincidence of this pulse
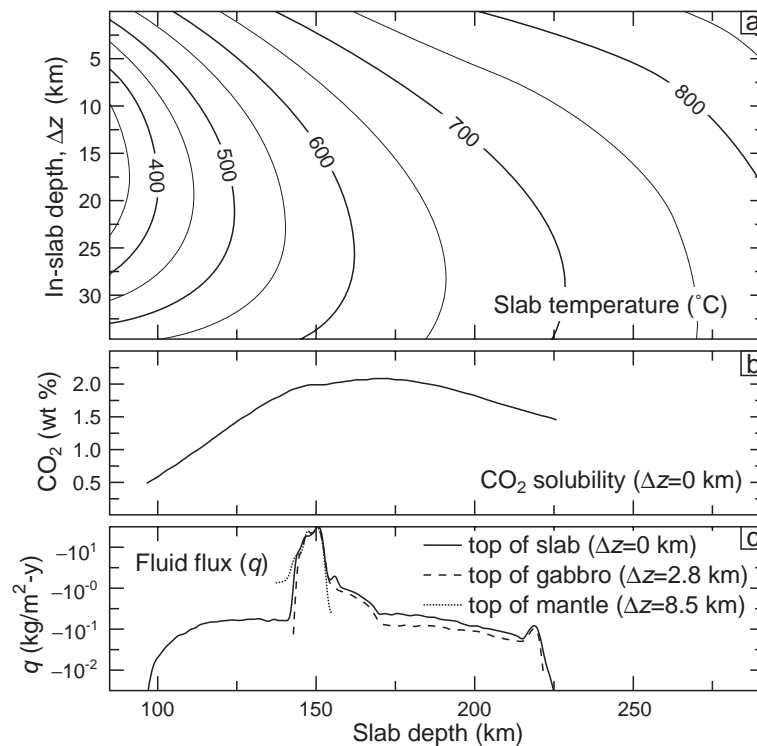

Fig. 7. Subduction zone devolatilization model conditions and results: (a) geothermal conditions within the subducted oceanic lithosphere obtained algebraically, assuming a parabolic vertical gradient, from geothermal gradients at the slab interface and at orthogonal depths of 8 and 25 km from the slab interface [24]; (b) equilibrium CO_2 concentration in the fluid at the slab interface; (d) fluid fluxes at the slab interface, at the base of the upper crust, and at the mantle-crust interface. In certain depth intervals, fluid fluxes do not increase upward through the slab because of local hydration reactions, most notably those responsible for forming phase-A in the mantle and talc in the lower crust commencing at slab depths of ~133 km (Figs. 8 and 9a). The integrated CO_2 flux is 4700 kg/m-y, assuming this value is representative of global subduction, and taking the global subduction rate to be 2.7 km^2/y, subduction zone devolatilization would release ~0.13 Gt CO_2/y, comparable to estimates of CO_2 release by island arc volcanism (0.09–0.11 Gt CO_2/y [55]).
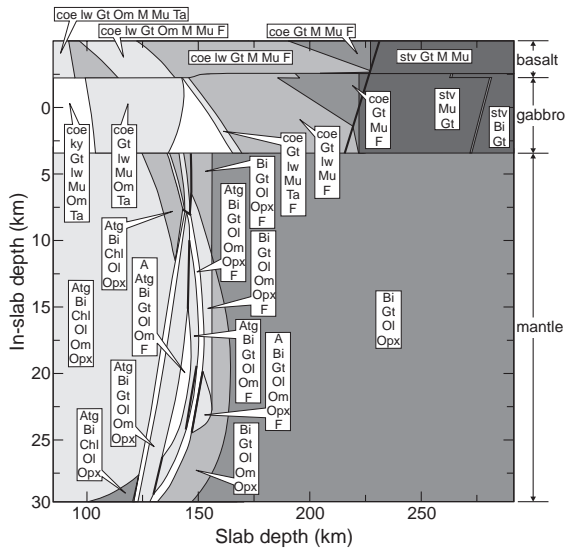
Fig. 8. Phase relations of subducted oceanic lithosphere ("slab") as a function of depth to the top of the slab and depth within the slab, see Figs. 6 and 7 for model geometry and conditions, and Table 1 for phase notation and data sources. Clinopyroxene is stable in all phase fields; at shallow slab depths two clinopyroxene phases coexist, only the presence of the more omphacitic phase (Om) is noted; other phases are stable as indicated. Univariant fields are indicated by heavy solid lines. Unlabeled phase fields can be deduced from the Maessing–Palatnik rule [23] that adjacent phase fields differ by the gain or loss of exactly one phase, although technically the diagram is not a phase diagram section. Pressure is related to depth assuming lithostatic conditions and a density of 3500 kg/m^3. The phase relations are those of a vertical column discretized at 50 m intervals. Equilibrium phase relations were computed from the base of the column upward, after each computation the mass of fluid evolved was subtracted from the local node and added to the overlying node to simulate fluid expulsion. Once phase relations though the entire column were computed, the physical conditions within the column were incremented to simulate 345 m of burial by subduction. Phase compositions were resolved with a maximum error of 0.15 mol% ($1.7 \cdot 10^5$ pseudocompounds) and the calculation required 6.5 h on a 1.5 GHz computer. Input files for this calculation are at www.per-plex.ethz.ch/perplex_examples.html#example_22.

with the maxima in CO_2 solubility (Fig. 7b) within the oceanic crust creates optimal conditions for infiltration driven decarbonation, yet the crustal carbonate content is reduced by only 23%.

Despite the complexity of the model scenario there are reasons to expect that the model provides a conservative estimate for carbon retention. The model mantle-water content (4 wt.% through the upper 18.5 km) is roughly one half that which might be achieved at oceanic trenches (8 wt.%, Fig. 5). Al-

though the foci of subduction zone seismic events suggest some mantle hydration (e.g., [32]), even the moderate water content assumed here has profound effects on the subduction zone seismic velocity structure (Fig. 9cd). Most notably, hydration lowers the mantle seismic velocity (e.g., [51]) with the result that the oceanic crust would act as a high velocity wave guide at sub-arc depths, in contrast to common observation that the oceanic crust appears to act as a low velocity wave guide (e.g., [52]). If the requirement that mantle seismic velocities be greater than those in oceanic crust is introduced as a constraint on the extent of mantle hydration, then an upper limit of ~2 wt.% is indicated for the average water content of the subjacent mantle. The amount of CO_2 present in the oceanic crust is not an important factor provided the carbonate content of the crust at the slab interface is not affected by infiltration; with this proviso the CO_2 loss by the slab is simply the product of the water flux with the CO_2 solubility at the slab interface. The solubility varies with temperature, but is only weakly dependent on bulk chemistry for the marine sediments and basaltic rocks that are likely to be the primary carbonate hosts in subduction zones [30,31]. The maxima in CO_2 solubility as a function of depth is a consequence of the steepening of the geotherm along the slab interface, as the vigor of mantle wedge convection reaches a steady-state [47,24], relative to the temperature-depth trajectory of the equilibrium solubility isopleths. The slopes of these isopleths vary remarkably little for the various subduction zone lithologies [30,31], thus the existence of a maximum in CO_2 solubility at ~140–160 km depth is likely to be a general feature. However, the temperature at this depth, and therefore the magnitude of the solubility, is uncertain. Thermo-mechanical model configurations [47] that incorporate a shear heating term at shallow depth lead to temperatures ~100 °C higher than those along the slab geotherm employed here. A temperature increase of this magnitude, would raise the maximum solubility to ~11 wt.% CO_2, thereby causing a five-fold increase in the efficiency of infiltration driven decarbonation, whereas a comparable decrease would reduce the maximum solubility to ~0.8 wt.%. The final major source of variability is the depth of mantle dehydration relative to this maximum, which is controlled by the geotherm within the oceanic slab and therefore strongly correlated to sub-
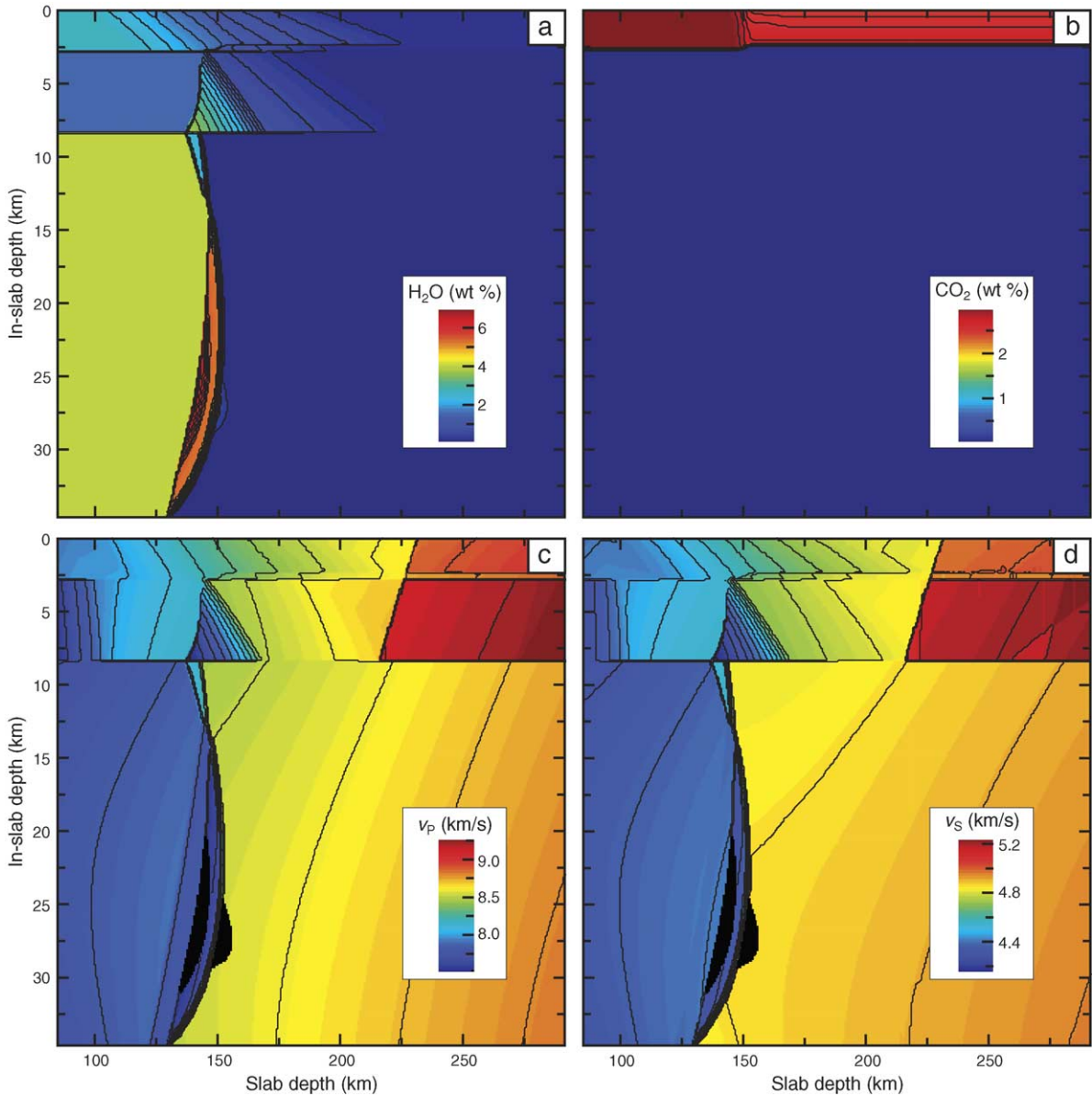
Fig. 9. Computed volatile-content and seismic velocities of the equilibrium slab mineralogy as a function depth to the top of the slab and depth within the slab. Contour intervals for water-content (a), CO_2 content (b), compressional-wave velocity (c) and shear-wave velocity (d) are 0.25 wt.%, 0.1 wt.%, 0.1 km/s and 0.05 km/s. Seismic velocities were computed using the shear modulus data base and methods described in [10], modified or augmented by shear modulus data for antigorite, olivine [56], clinopyroxene [56], orthopyroxene [56], and biotite [8]. In the case of antigorite, the shear modulus as a function of pressure and temperature was derived from estimates for shear- and compressional-wave velocities of serpentinite [51] using the adiabatic bulk modulus computed from [3]. Seismic velocities were not computed in stability field of phase-A, the black areas at in-slab of depths 17–30 km and slab depths of 130–155 km. The synthetic tomographic images (c, d) are inconsistent with the observation that the crust is characterized by low velocities relative to the underlying mantle to >150 km depth [e.g., [52]]. This inconsistency suggests that the water content of the model mantle is excessive. As noted previously [10], high velocities caused by the presence of stishovite in the subducted crust at slab-depths beyond 220 km (Fig. 8) correlate well with the deep high-velocity anomaly at the Tonga–Kermadec subduction zone [57].

duction rate. Steeper geothermal gradients, delay mantle dehydration to greater depths where phase-A is stabilized, thereby reducing the amount of water available to extract CO_2 [24]. Lower gradients, would allow more complete mantle dehydration at shallower depths, but the increased water flux would be countered by the reduction in CO_2 solubility at these depths. Thus, repetition of the model calculation for a subduction rate of 2 cm/y results in results in lower relative (13.3%) and absolute (545 kg/m-y) carbon loss.

The foregoing considerations suggest that the earlier conclusion [30,31], based on closed system models for decarbonation, that carbonates are likely to persist within the subducted oceanic crust beyond sub-arc depths is robust. As anticipated, the effect of open system behavior is to increase carbonate stability in the absence of an external source of water. However, even in the model as configured here to maximize infiltration driven decarbonation, 40–90% of the total carbonate is retained beyond sub-arc depths. Current thermodynamic models for silicate melts do not account for CO_2 solubility, and therefore the potential effect of melting cannot be assessed here. Experimental work (J. Hermann, personal communication, 2004) suggests that granitic melts generated by slab melting may be a vehicle for removing carbonate; however the experiments are for closed system melting and give volatile fractions that are lower than obtained in thermodynamic models for closed system devolatilization in the absence of melting. Thus, although melts may well be the real mechanism for volatile transfer from the slab, they are a more effective transfer mechanism only in the sense that once formed they may persist within the slab longer than low-density aqueous fluids, thereby leading to a closer approximation of closed system decarbonation.

6. Discussion

Phase relations exert a first order control on rock properties and therefore knowledge of phase relations and their physical consequences are essential for understanding geodynamic processes. This paper outlines a simple scheme for obtaining such information from thermodynamic data. The scheme consists of a free energy minimization method for computing the stable state of a system at any arbitrary condition, and a strategy by which the minimization technique is applied to map phase relations and physical properties as a function of the variables of interest. Linearization of the free energy minimization problem as advocated here is arguably a retrogressive step in light of developments in optimization algorithms (e.g., [17,9,53]); however given technological advances such crude techniques merit reexamination. The value of the linearized solution is that it is easily implemented, is absolutely stable, and requires no tuning to accommodate the various specialized equations of state used in geosciences. The applications to melting problems illustrated here demonstrate the feasibility of treating relatively complex phases by this technique. However these applications are at the limits imposed by current technology, routine treatment of phases with more than nine degrees of compositional freedom or even the accurate resolution of trace quantities of species require more sophisticated approaches. In this regard, iterative refinement of the linearized solution may offer a practical alternative to non-linear solution techniques.

The mapping and storage of information from phase diagram sections provides a means by which geodynamic or geophysical models can be passively coupled to phase equilibrium constraints. In principle, such passive coupling can be done for geodynamic models of any degree of complexity provided phase relations can be mapped as a function of geodynamic variables. However, mapping as a function of three or more variables, as required by geodynamic models in which variations in physical conditions as well as mass transfer occur, is currently too costly to be practical. Such problems can be addressed by dynamic coupling of geodynamic and phase equilibrium calculations or if the phase equilibrium calculations are done for a prescribed geodynamic scenario, as illustrated by the model presented here for subduction zone decarbonation.

The subduction zone decarbonation model was designed to assess the extent to which decarbonation of the upper portion of the subducted oceanic crust may be driven by infiltration of water-rich fluids derived by dehydration of the lower crust and mantle. In this regard, it was formulated to evaluate the extreme scenario of instantaneous fluid expulsion, in which fluids nonetheless are able to equilibrate fully

with the rocks they pass through. The model represents a limiting case for the efficiency of open system decarbonation. Expected deviations from this model in natural systems, such as those caused by flow channelization or kinetically inhibited devolatilization, would lead to behavior represented by the limiting case of batch or closed system devolatilization. The solubility of CO_2 in aqueous fluids in equilibrium with the upper portion of subducted oceanic crust exerts a fundamental control on decarbonation and is primarily a function of temperature. Subduction zone geotherms steepen at sub-arc depths, as heat-loss due to mantle convection approaches a steady state, resulting in a maximum CO_2 solubility that is typically in the range 1–10 wt.% [30,31]. Thus, given that the mass ratio of CO_2 to water within the oceanic crust is not likely to be much less than one, the best case scenario for infiltration-driven decarbonation is that a large influx of mantle derived water occurs at the depth of maximum CO_2 solubility. The seismic velocity profiles computed here for the subduction zone model, together with the limit on the depth of mantle hydration imposed by the stability of antigorite, imply a maximum water-content of the subducted mantle of $\sim 1.7 \ 10^7 \ kg/m^2$. For the aforementioned solubilities, this quantity of water is capable of scavenging 0.25-2.5 wt.% CO_2 from the upper 2 km of the oceanic crust. This simple analysis constrains the upper limit on the efficacy of infiltration decarbonation. In view of this analysis, the persistence a large fraction of the initial slab carbonate budget beyond sub-arc depths, as illustrated by the specific the subduction zone decarbonation model presented here, is plausible even if the upper portion of the slab is infiltrated by water-rich fluids derived by subjacent dehydration.

Acknowledgements

References

[1] J.W. Johnson, E.H. Oelkers, H.C. Helgeson, SUPCRT92: a software package for calculating the standard molal thermodynamic properties of minerals, gases, aqueous species, and reactions from 1 to 5000 bar and 0 to 1000 °C, Comput. Geosci. 18 (1992) 899–947.

[2] R.G. Berman, L.Y. Aranovich, Optimized standard state and solution properties of minerals: I. Model calibration for olivine, orthopyroxene, cordierite, garnet and ilmenite in the system FeO–MgO–CaO–Al_2O_3–TiO_2–SiO_2, Contrib. Mineral. Petrol. 126 (1996) 1–24.

[3] T.J.B. Holland, R. Powell, An internally consistent thermodynamic data set for phases of petrological interest, J. Metamorph. Geol. 16 (1998) 309–343.

[4] M. Gottschalk, Internally consistent thermodynamic data for rock forming minerals, Eur. J. Mineral. 9 (1997) 175–223.

[5] L. Stixrude, C. Lithgow-Bertelloni, Mineralogy and elasticity of the oceanic upper mantle: origin of the low-velocity zone, J. Geophys. Res. 110 (2005) (art. no.-2965).

[6] R.W. White, R. Powell, T.J.B. Holland, Calculation of partial elting equilibria in the system Na_2O–CaO–K_2O–FeO–MgO–Al_2O_3–SiO_2–H_2O (NCKFMASH), J. Metamorph. Geol. 19 (2001) 139–153.

[7] M.S. Ghiorso, M.M. Hirschmann, P.W. Reiners, V.C. Kress, The pMELTS: a revision of MELTS for improved calculation of phase relations and major element partitioning related to partial melting of the mantle to 3 GPa, Geochem. Geophys. Geosystems 3 (2002) (art. no.-1030).

[8] S.V. Sobolev, A.Y. Babeyko, Modeling of mineralogical composition, density, and elastic-wave velocities in anhydrous magmatic rocks, Surv. Geophys. 15 (1994) 515–544.

[9] C.R. Bina, Free energy minimization by simulated annealing with applications to lithospheric slabs and mantle plumes, Pure Appl. Geophys. 151 (1998) 605–618.

[10] J.A.D. Connolly, D.M. Kerrick, Metamorphic controls on seismic velocity of subducted oceanic crust at 100–250 km depth, Earth Planet. Sci. Lett. 204 (2002) 61–74.

[11] C.R. Bina, S. Stein, F.C. Marton, E.M. Van Ark, Implications of slab mineralogy for subduction dynamics, Phys. Earth Planet. Inter. 127 (2001) 51–66.

[12] K. Petrini, J.A.D. Connolly, Y.Y. Podladchikov, A coupled petrological–tectonic model for sedimentary basin evolution: the influence of metamorphic reactions on basin subsidence, Terra Nova 13 (2001) 354–359.

[13] T.V. Gerya, W.V. Maresch, A.P. Willner, D.D. Van Reenen, C.A. Smit, Inherent gravitational instability of thickened continental crust with regionally developed low- to medium-pressure granulite facies metamorphism, Earth Planet. Sci. Lett. 190 (2001) 221–235.

[14] L.H. Rupke, J.P. Morgan, M. Hort, J.A.D. Connolly, Are the regional variations in Central American arc lavas due to differing basaltic versus peridotitic slab sources of fluids? Geology 30 (2002) 1035–1038.

[15] S.K. Saxena, G. Eriksson, Theoretical computation of mineral assemblages in pyrolite and lherzolite, J. Petrol. 24 (1983) 538–555.

[16] B.J. Wood, J.R. Holloway, A thermodynamic model for subsolidus equilibria in the system CaO–MgO–Al$_2$O$_3$–SiO$_2$, Geochim. Cosmochim. Acta 66 (1984) 159–176.

[17] C. DeCapitani, T.H. Brown, The computation of chemical equilibria in complex systems containing non-idel solutions, Geochim. Cosmochim. Acta 51 (1987) 2639–2652.

[18] W.B. White, S.M. Johnson, G.B. Dantzig, Chemical equilibrium in complex mixtures, J. Chem. Phys. 28 (1958) 751–755.

[19] J.A.D. Connolly, D.M. Kerrick, An algorithm and computer-program for calculating composition phase-diagrams, Calphad–Computer Coupling of Phase Diagrams and Thermochemistry 11 (1987) 1–55.

[20] J.P. Ignizio, Linear Programming in Single- and Multiple-Objective Systems, Prentice-Hall, 1982, (506 pp.).

[21] F. Van Zeggeren, S.H. Storey, The Computation of Chemical Equilibria, Cambridge University Press, Cambridge, 1970.

[22] O.V. Vasilyev, T.V. Gerya, D.A. Yuen, The application of multidimensional wavelets to unveiling multi-phase diagrams and in situ physical properties of rocks, Earth Planet. Sci. Lett. 223 (2004) 49–64.

[23] J.A.D. Connolly, K. Petrini, An automated strategy for calculation of phase diagram sections and retrieval of rock properties as a function of physical conditions, J. Metamorph. Petrol. 20 (2002) 697–708.

[24] L.H. Rupke, J.P. Morgan, M. Hort, J.A.D. Connolly, Serpentine and the subduction zone water cycle, Earth Planet. Sci. Lett. 223 (2004) 17–34.

[25] R.A. Berner, A.C. Lasaga, Modeling the geochemical carbon-cycle, Sci. Am. 260 (1989) 74–81.

[26] D.M. Kerrick, K. Caldeira, Paleoatmospheric consequences of CO$_2$ released during early Cenozoic regional metamorphism in the Tethyan orogen, Chem. Geol. 108 (1993) 201–230.

[27] J. Selverstone, D.S. Gutzler, Post-125 Ma carbon storage associated with continent–continent collision, Geology 21 (1993) 885–888.

[28] G.E. Bebout, The impact of subduction-zone metamorphism on mantle–ocean chemical cycling, Chem. Geol. 126 (1995) 191–218.

[29] D.M. Kerrick, J.A.D. Connolly, Subduction of ophicarbonates and recycling of CO$_2$ and H$_2$O, Geology 26 (1998) 375–378.

[30] D.M. Kerrick, J.A.D. Connolly, Metamorphic devolatilization of subducted oceanic metabasalts: implications for seismicity, arc magmatism and volatile recycling, Earth Planet. Sci. Lett. 189 (2001) 19–29.

[31] D.M. Kerrick, J.A.D. Connolly, Metamorphic devolatilization of subducted marine sediments and the transport of volatiles into the Earth's mantle, Nature 411 (2001) 293–296.

[32] B.R. Hacker, S.M. Peacock, G.A. Abers, S.D. Holloway, Subduction factory-2. Are intermediate-depth earthquakes in subducting slabs linked to metamorphic dehydration reactions? J. Geophys. Res.-Solid Earth 108 (2003) (art. no.-2030).

[33] D. Kerrick, Serpentinite seduction, Science 298 (2002) 1344–1345.

[34] J.A.D. Connolly, Multivariable phase-diagrams—an algorithm based on generalized thermodynamics, Am. J. Sci. 290 (1990) 666–718.

[35] V.M. Goldschmidt, Geochemistry, Clarendon Press, Oxford, 1954, (730 pp.).

[36] R. Powell, T.J.B.H. Holland, B. Worley, Calculating phase diagrams involving solid solutions via non-linear equations, with examples using THERMOCALC, J. Metamorph. Geol. 16 (1998) 577–588.

[37] M.S. Ghiorso, R.O. Sack, Chemical mass-transfer in magmatic processes: 4. A revised and internally consistent thermodynamic model for the interpolation and extrapolation of liquid–solid equilibria in magmatic systems at elevated temperatures and pressures, Contrib. Mineral. Petrol. 19 (1995) 197–212.

[38] P.D. Asimow, M.M. Hirschmann, E.M. Stolper, Calculation of peridotite partial melting from thermodynamic models of minerals and melts: IV. Adiabatic decompression and the composition and mean properties of mid-ocean ridge basalts, J. Petrol. 42 (2001) 963–998.

[39] I.K. Karpov, K.V. Chudnenko, D.A. Kulik, Modeling chemical mass transfer in geochemical processes: thermodynamic relations, conditions of equilibria, and numerical algorithms, Am. J. Sci. 297 (1997) 767–806.

[40] R. Dasgupta, M.M. Hirschmann, A.C. Withers, Deep global cycling of carbon constrained by the solidus of anhydrous, carbonated eclogite under upper mantle conditions, 227 (2004) 73-85.

[41] J.A.D. Connolly, V. Trommsdorff, Petrogenetic grids for metacarbonate rocks—pressure–temperature phase-diagram projection for mixed-volatile systems, Contrib. Mineral. Petrol. 108 (1991) 93–105.

[42] H. Staudigel, S. Hart, H. Schmincke, B. Smith, Cretaceous ocean crust at DSDP sites 417–418: carbon uptake from weathering versus loss by magmatic outgassing, Geochim. Cosmochim. Acta 53 (1989) 3091–3094.

[43] M.D. Behn, P.B. Kelemen, Relationship between seismic P-wave velocity and the composition of anhydrous igneous and meta-igneous rocks, Geochem. Geophys. Geosystems 4 (2003) (art. no.-1041).

[44] R.L. Carlson, Bound water content of the lower oceanic crust estimated from modal analyses and seismic velocities of oceanic diabase and gabbro, Geophys. Res. Lett. 30 (2003) (art. no.-2142).

[45] S.R. Hart, A. Zindler, In search of a bulk-earth composition, Chem. Geol. 57 (1986) 247–267.

[46] F.A. Dahlen, Metamorphism of nonhydrostatically stressed rocks, Am. J. Sci. 292 (1992) 184–198.

[47] P.E. van Keken, B. Kiefer, S.M. Peacock, High-resolution models of subduction zones: implications for mineral dehydration reactions and the transport of water into the deep mantle, Geochem. Geophys. Geosystems 3 (2002) (art. no.-1056).

[48] T. Plank, C.H. Langmuir, The chemical composition of subducting sediment and its consequences for the crust and mantle, Chem. Geol. 145 (1998) 325–394.

[49] S.M. Peacock, Large-scale hydration of the lithosphere above subducting slabs, Chem. Geol. 108 (1993) 49–59.

[50] M.W. Schmidt, S. Poli, Experimentally based water budgets for dehydrating slabs and consequences for arc magma generation, Earth Planet. Sci. Lett. 163 (1998) 361–379.

[51] R.L. Carlson, D.J. Miller, Mantle wedge water contents estimated from seismic velocities in partially serpentinized peridotites, Geophys. Res. Lett. 30 (2003) (art. no.-1250).

[52] G. Abers, Seismic low-velocity layer at the top of subducting slabs: observations, predictions, and systematics, Phys. Earth Planet. Inter. 149 (2005) 7–29.

[53] I.K. Karpov, K.V. Chudnenko, D.A. Kulik, O.V. Avchenko, V.A. Bychinskii, Minimization of Gibbs free energy in geochemical systems by convex programming, Geochem. Int. 39 (2001) 1108–1119.

[54] D.M. Shaw, Geochemistry of pelite rocks: III. major elements and general geochemistry, Geol. Soc. Amer. Bull. 67 (1956) 919–934.

[55] D.M. Kerrick, Present and past nonanthropogenic CO_2 degassing from the solid Earth, Rev. Geophys. 39 (2001) 565–585.

[56] P. Vacher, A. Mocquet, C. Sotin, Computation of seismic profiles from mineral physics: the importance of the non-olivine components for explaining the 660 km depth discontinuity, Phys. Earth Planet. Inter. 106 (1998) 275–298.

[57] D. Gubbins, A. Barnicoat, J. Cann, Seismological constraints on the gabbro–eclogite transition in subducted oceanic crust, Earth Planet. Sci. Lett. 122 (1994) 89–101.

[58] R. Powell, T. Holland, Relating formulations of the thermodynamics of mineral solid solutions: activity modeling of pyroxenes, amphiboles, and micas, Am. Mineral. 84 (1999) 1–14.

[59] T. Holland, J. Baker, R. Powell, Mixing properties and activity–composition relationships of chlorites in the system $MgO–FeO–Al_2O_3–SiO_2–H_2O$, Eur. J. Mineral. 10 (1998) 395–406.

[60] T. Holland, R. Powell, Thermodynamics of order–disorder in minerals: 2. Symmetric formalism applied to solid solutions, Am. Mineral. 81 (1996) 1425–1437.

[61] M.L. Fuhrman, D.H. Lindsley, Ternary-feldspar modeling and thermometry, Am. Mineral. 73 (1988) 201–215.

[62] R.C. Newton, T.V. Charlu, O.J. Kleppa, Thermochemistry of the high structural state plagioclases, Geochem. Cosmochim. Acta 44 (1980) 933–941.

[63] J.B. Thompson, G.L. Hovis, Entropy of mixing in sanidine, Am. Mineral. 64 (1979) 57–65.

[64] C.J. Wei, R. Powell, Phase relations in high-pressure metapelites in the system KFMASH ($K_2O–FeO–MgO–Al_2O_3–SiO_2–H_2O$) with application to natural rocks, Contrib. Mineral. Petrol. 145 (2003) 301–315.